Published in final edited form as:
Comput Methods Biomech Biomed Engin. 2014 ; 17(6): 604–615. doi:10.1080/10255842.2012.704368.

Improved discretisation and linearisation of active tension in strongly coupled cardiac electro-mechanics simulations

J. Sundnes[a,*], **S. Wall**[a], **H. Osnes**[b], **T. Thorvaldsen**[c], and **A.D. McCulloch**[d]

[a]Simula Research Laboratory, Lysaker, Norway/Department of Informatics, University of Oslo, Oslo, Norway

[b]Department of Mathematics, University of Oslo, Oslo, Norway

[c]Norwegian Defense Research Establishment, Kjeller, Norway

[d]Department of Bioengineering, University of California, San Diego, La Jolla, CA, USA

Abstract

Mathematical models of cardiac electro-mechanics typically consist of three tightly coupled parts: systems of ordinary differential equations describing electro-chemical reactions and cross-bridge dynamics in the muscle cells, a system of partial differential equations modelling the propagation of the electrical activation through the tissue and a nonlinear elasticity problem describing the mechanical deformations of the heart muscle. The complexity of the mathematical model motivates numerical methods based on operator splitting, but simple explicit splitting schemes have been shown to give severe stability problems for realistic models of cardiac electro-mechanical coupling. The stability may be improved by adopting semi-implicit schemes, but these give rise to challenges in updating and linearising the active tension. In this paper we present an operator splitting framework for strongly coupled electro-mechanical simulations and discuss alternative strategies for updating and linearising the active stress component. Numerical experiments demonstrate considerable performance increases from an update method based on a generalised Rush–Larsen scheme and a consistent linearisation of active stress based on the first elasticity tensor.

Keywords

cardiac electro-mechanics; strongly coupled simulation; operator splitting

1. Introduction

The pumping of the heart is the result of a complex interaction between electro-chemical reactions in the heart cells, passive mechanical properties of the heart muscle tissue and the haemodynamics of the circulatory system. Given the clinical importance of the heart, it is not surprising that all of these processes have been studied extensively. As a result, we now have detailed knowledge of these processes covering the full range of spatial scales, from

*Corresponding author. sundnes@simula.no.

sub-cellular all the way to the complete organ level. However, in spite of these advances, much is still unknown, both of certain critical processes such as cross-bridge interaction and cooperative mechanisms (see for instance Rice and deTombe 2004). Development of detailed mathematical models for each process, which can be combined into complete computational models of heart electro-mechanics, is a valuable research activity for advancing this knowledge further. However, although remarkable progress has been achieved in this area, the development is slowed by the complexity and multi-scale nature of the equations, and the lack of efficient computational methods for full-scale heart modelling.

When modelling the contracting heart muscle, it is convenient to view the process as consisting of three tightly integrated parts: (i) electro-chemical reactions in the cardiac myocytes, causing cross-bridge cycling and active tension development in the cells; (ii) conduction of the electrical signal from cell to cell by means of membrane depolarisation and (iii) deformation caused by the balance of contractile forces, passive mechanical properties of tissue and loading induced by the blood pressure inside the cavities. Very detailed and accurate mathematical models exist for all these parts. On the cellular level, electrophysiological states such as membrane channels and ionic concentrations are described in impressive detail, and, although they have to some extent lagged behind the electrophysiology models, models of myofilament interaction and force development are becoming increasingly accurate. The CellML web page (2012) provides an extensive repository of both electro-physiology and contraction models. On a tissue level, models based on the bidomain concept have been widely accepted as descriptions of cardiac activation (see e.g. Lines et al. 2002), whereas the mechanical deformations can be described by the fundamental laws of continuum mechanics. A wide range of constitutive relations have been developed for the material behaviour of the muscle (see e.g. Holzapfel and Ogden 2009 for a recent example).

The mathematical models for the various processes may be readily coupled together, but solving the resulting systems of differential equations remains a challenge. Examples of coupled electro-mechanics simulations in the literature employ a variety of different solution methods. Some studies have employed advanced models for the mechanics, but computed the activation sequence prior to and independently from the deformations (Usyk et al. 2002; Kerckhoffs et al. 2003). Others have solved the problem fully coupled, including mechano-electric feedback, but have used simplified models both for electrophysiology and mechanical properties (see Nash and Panfilov 2004). In Nickerson et al. (2005), the electrophysiology and mechanics equations were solved in a coupled manner using biophysically detailed models for cellular reactions and contraction. An improved computational method for strongly coupled simulations was presented by Niederer and Smith (2008), targeting the contraction model of Niederer et al. (2006), whereas Pathmanathan and Whiteley (2009) present a different algorithm for the same contraction model. Other studies, Campbell et al. (2009) and Gurev et al. (2011a, 2011b), have presented strongly coupled simulations based on the contraction model of Rice et al. (2008), and Göktepe and Kuhl (2009) have presented a fully implicit solution scheme for coupled cardiac electro-mechanics. Recent studies (Land et al. 2012; Lafortune et al. 2012) have studied computational efficiency of electro-mechanical simulations on different computational architectures.

The aim of this paper was to present an operator splitting framework for computer simulations of strongly coupled cardiac electro-mechanics and to discuss alternative solution methods for the resulting sub-problems. The splitting method separates the overall model into three tightly linked sub-problems corresponding to (i)–(iii) above and combines sub-problem solutions to obtain a robust solution method for the coupled problem. The main focus of the paper is on deriving stable and accurate schemes for solving the mechanics sub-problem, and we mainly focus on the contraction model of Rice et al. (2008). This model features a different deformation–force feedback formulation from Niederer et al.'s (2006) model and related contraction models. The added detail and complexity of the feedback model gives rise to additional challenges in deriving a stable solution scheme.

The paper is organised as follows. In Section 2, we describe the mathematical models for the three subprocesses included in the modelling and show how they are coupled to form a complete mathematical model. In Section 3, the proposed numerical method is presented, with emphasis on methods for the mechanics sub-problem. Section 4 presents numerical results to investigate the performance of the alternative methods, whereas Section 5 contains a short summary and concluding remarks.

2. Mathematical model

The mathematical model for cardiac electro-mechanics can be written as a system of ordinary differential equations (ODEs) and partial differential equation (PDEs):

$$\frac{\partial \mathbf{s}}{\partial t} = f(v, \mathbf{s}, \lambda), \quad \mathbf{x} \in H, \quad (1)$$

$$\frac{\partial v}{\partial t} + I_{\text{ion}}(v, \mathbf{s}, \lambda) = \nabla \cdot (\mathbf{M}_i \nabla v) + \nabla \cdot (\mathbf{M}_i \nabla u_e), \quad \mathbf{x} \in H, \quad (2)$$

$$\nabla \cdot ((\mathbf{M}_i + \mathbf{M}_e) \nabla u_e) = -\nabla \cdot (\mathbf{M}_i \nabla v), \quad \mathbf{x} \in H, \quad (3)$$

$$\nabla \cdot (\mathbf{F}\mathbf{S}) = 0, \quad \mathbf{x} \in H, \quad (4)$$

with the constitutive relations

$$\mathbf{S} = \mathbf{S}^{\text{p}} + \mathbf{S}^{\text{a}}, \quad (5)$$

$$\mathbf{S}^{\text{p}} = \frac{\partial \Psi}{\partial \mathbf{E}}, \quad (6)$$

$$\mathbf{S}^{\text{a}} = J\mathbf{F}^{-1}\boldsymbol{\sigma}^{\text{a}}(\mathbf{s}, \lambda, \dot{\lambda})\mathbf{F}^{-T}, \quad (7)$$

and the boundary conditions

$$\boldsymbol{\eta} \cdot (\mathbf{M}_i \nabla v + \mathbf{M}_i \nabla u_e) = 0, \quad \mathbf{x} \in \partial H, \quad (8)$$

$$\boldsymbol{\eta} \cdot (\mathbf{M}_e \nabla u_e) = 0, \quad \mathbf{x} \in \partial H, \quad (9)$$

$$\mathbf{u} = 0, \quad \mathbf{x} \in \partial H_1, \quad (10)$$

$$\mathbf{T} = J \overline{\sigma}_1 \mathbf{F}^{-T} \cdot \boldsymbol{\eta}, \quad \mathbf{x} \in \partial H_2, \quad (11)$$

$$\mathbf{T} = J \overline{\sigma}_2(t) \mathbf{F}^{-T} \cdot \boldsymbol{\eta}, \quad \mathbf{x} \in \partial H_3. \quad (12)$$

In the above equations, the system of ODEs for cell electrophysiology and excitation–contraction coupling is given by (1), where **s** is the vector of state variables at time *t*, typically describing membrane channels and intracellular ionic concentrations. The transmembrane potential v is the difference between the intracellular potential u_i and the extracellular potential u_e, and λ is the fibre extension ratio, i.e. the current sarcomere length divided by the slack length. A comprehensive overview of cell electrophysiology and mechanics is found on the CellML web page (2012). Models for active force development include simple models like the model applied by Nash and Panfilov (2004), as well as more detailed contraction models like the Hunter–McCulloch–ter Keurs (HMT) model (see Hunter et al. 1998) and the model by Rice et al. (2008). The cell electromechanics models obtained by combining these two types of models show large variations in complexity due to their physiological level of detail. For instance, the model applied by Nash and Panfilov consists of only three ODEs, whereas the main model addressed in this paper has 40 ODEs. This model results from combining the model of Winslow et al. (1999) for cell electrophysiology with the model of Rice et al. (2008) for force development. Some numerical results are presented for a model which combines Winslow et al.'s model with the HMT model for mechanics, resulting in a system of 32 ODEs. In brief, the coupled electro-mechanics model is formed by taking intracellular calcium predicted by the electrophysiology model as input to the contraction model. Since the binding of Ca to Troponin C (TnC) is described by all three models, there is some redundancy in the coupled model which needs to be resolved. For coupling Winslow et al.'s model to the HMT model, we have used calcium binding equations from Winslow et al.'s model, but modified for stretch dependence according to the HMT model. Rice et al.'s model uses two ODEs to describe Ca^{2+} binding to TnC, and in the coupled model we have replaced the single equation in Winslow et al.'s model by these two. Several alternative coupled models exist as described, for instance, in Nickerson et al. (2001), Campbell et al. (2009) and Gurev et al. (2011a, 2011b).

The propagation of the electrical pulse is described by bidomain model, (2) and (3) (Tung 1978). Here, I_{ion} is the total ionic current, which has been scaled with the membrane capacitance. Moreover, $\mathbf{M}_i$ and $\mathbf{M}_e$ are the intracellular and extracellular conductivity tensors, respectively, which have been scaled with the membrane capacitance and the cell

membrane area to volume ratio (see, for instance, Sundnes et al. 2005, 2006, for details on the scaling). For simplicity we consider an isolated heart, where the no-flux boundary conditions (8) and (9) apply to the complete boundary. Also note that (2) and (3) are solved on the undeformed geometry, and we do not consider the effect of deformation on the tissue conductivity, as described by Nash and Panfilov (2004).

The mechanical behaviour is described by the equilibrium Equation (4), combined with the constitutive relations (5)–(7). Here **F** is the deformation gradient, whereas **S** is the second Piola–Kirchhoff stress tensor. A total Lagrangian formulation is employed in (4), in which all quantities are mapped back to the reference geometry H (i.e. at $t = 0$; see e.g. Holzapfel 2000). As expressed in (5), the second Piola–Kirchhoff stress tensor is written as a sum of a passive part $\mathbf{S}^{\mathrm{p}}$ and an active part $\mathbf{S}^{\mathrm{a}}$. Assuming that the myocardium can be modelled as a hyperelastic material, the passive part of the second Piola–Kirchhoff stress tensor (6) is defined as the first derivative of the strain energy function $\boldsymbol{\Psi}$ with respect to the components of the Green–Lagrange strain tensor. Examples of widely used models for passive tissue behaviour can be found in Guccione et al. (1995), Hunter et al. (1998), Usyk et al. (2000) and Holzapfel and Ogden (2009). For the numerical experiments presented in this paper, we have employed the transversely isotropic version of the exponential strain energy function from Usyk et al. (2002):

$$\Psi=\frac{1}{2}C(\mathrm{e}^{W}-1)+C_{\mathrm{compr}}(J\ln J-J+1), \quad (13)$$

$$W=b_{ff}E_{ff}^{2}+b_{xx}\left(E_{ss}^{2}+E_{nn}^{2}+E_{sn}^{2}+E_{ns}^{2}\right)+b_{fx}\left(E_{fn}^{2}+E_{nf}^{2}+E_{fs}^{2}+E_{sf}^{2}\right). \quad (14)$$

Here C, C_{compr}, b_{ff}, b_{xx} and b_{fx} are material parameters, E_{ij} are components of the Green–Lagrange strain tensor **E** and J is the determinant of the deformation gradient **F**. The material is modelled as slightly incompressible, in which the penalty factor C_{compr} in (13) is adjusted to control the volume changes.

The active part of the second Piola–Kirchhoff stress tensor is expressed in (7), where $\boldsymbol{\sigma}^{\mathrm{a}}$ is the active Cauchy stress tensor. Referred to a local fibre coordinate system, only the normal stress components (i.e. the diagonal components) of the active Cauchy stress tensor are non-zero. The active force development in cardiac muscle is triggered by an increase in intracellular calcium concentration, which is contained in the state vector **s** described above. In addition, the force is known to depend on the extension ratio λ and its time derivative, denoted by $\dot{\lambda}$. As noted above, we compute the fibre tension from two alternative models: the HMT model and the model by Rice et al. (2008). The HMT model includes the reference tension T_{ref} as a model parameter, and we apply the same parameter to scale the normalised tension produced by the model of Rice et al. (2008). We refer to the original publications for the details on the active tension formulations. Although intuitively one will expect the force developed by the cardiac cells to be primarily directed in the direction of the fibres, experimental results indicate significant active forces in the transverse directions (see e.g.

Lin and Yin 1998). We compute the transverse stress components by introducing two additional material constants γ_s and γ_n, and setting $\sigma_{ss} = \gamma_s \sigma_{ff}$ and $\sigma_{nn} = \gamma_n \sigma_{ff}$.

For the mechanical part of the problem it is appropriate to divide the boundary into three disjoint sub-domains, $\partial H = \partial H_1 \cup \partial H_2 \cup \partial H_3$. We apply displacement con-ditions to certain parts of the boundary ∂H_1, an externally applied constant normal stress load $\bar{\sigma}_1$ to other parts ∂H_2, and a time-dependent externally applied normal stress load $\bar{\sigma}_2$ to the rest of the boundary ∂H_3, expressed by (10)–(12), respectively. Typically, the time-dependent normal stress load will be applied to the endocardial surface of the ventricle, to mimic the effect of the blood pressure for the different phases of the heart cycle. The temporal changes of blood pressure may be described by sophisticated closed-loop circulation models, as described in Kerckhoffs et al. (2007), but for this study we adopt a simpler approach. In the passive filling phase we apply a prescribed pressure increasing in time, while in the other phases the pressure depends on the deformation state, and has to be determined through an iterative procedure. In the isovolumic phases the pressure load must fulfil the constant cavity volume constraint, whereas in the ejection phase the pressure load (and cavity volume) is obtained from a two-element Windkessel model:

$$\frac{\mathrm{d}V}{\mathrm{d}t} = -C_{\mathrm{art}} \frac{\mathrm{d}p}{\mathrm{d}t} - \frac{p - p_0}{R_{\mathrm{per}}}, \quad (15)$$

where V is the cavity volume, p is the cavity pressure, C_{art} is the total arterial compliance, p_0 is the venous pressure and R_{per} is the total peripheral resistance. Furthermore, a constant normal stress load is often employed at the epicardial surface of the ventricle. Displacement restrictions are applied at certain points of the boundary to avoid rigid body motions. The normal vector η refers to the reference geometry H.

3. Numerical methods

In this section we introduce the operator splitting framework for solving the strongly coupled electromechanics problem. The solvers for the electro-physiology sub-problem are briefly described, while most of the section is devoted to methods for updating and linearising active tension. As shown in Niederer and Smith (2008), these steps are crucial for the efficiency and reliability of the numerical scheme.

3.1 Operator splitting

Equations (1)–(12) define a highly complex system of nonlinear ODEs and PDEs, for which it is difficult to design efficient solution techniques. Although examples of fully coupled splitting methods exist (see e.g. Göktepe and Kuhl 2009), the majority of published methods are based on some form of operator splitting (see e.g. Niederer and Smith 2008; Campbell et al. 2009; Gurev et al. 2011a, 2011b).

We propose a Gauss–Seidel approach to separate the nonlinear elasticity problem from the cellular reactions and the bidomain model. Moreover, a Godunov splitting is employed to separate the nonlinear ionic current term from the bidomain model, as described in Sundnes et al. (2005). The proposed approach results in an algorithm by which three sub-problems

are solved at each time step: a nonlinear ODE system for each nodal point describing cellular reactions (including both cell electrophysiology and the ODEs describing cross-bridge activation), a linear system of PDEs modelling propagation of the electrical signal and a nonlinear elasticity equation describing the mechanical deformations. Assuming that the fields v_n, $\mathbf{s}_n$ and $\mathbf{u}_n$ are known at time t_n, one time step of the algorithm can be written as follows:

1. Solve the ODE system

$$\frac{\mathrm{d}v}{\mathrm{d}t} = -I_{\mathrm{ion}}(v, \mathbf{s}, \lambda), \quad t_n < t \leq t_{n+1}, \quad v(t_n) = v_n, \quad (16)$$

$$\frac{\mathrm{d}\mathbf{s}}{\mathrm{d}t} = f(v, \mathbf{s}, \lambda), \quad t_n < t \leq t_{n+1}, \quad \mathbf{s}(t_n) = \mathbf{s}_n, \quad (17)$$

to determine the updated state vector s_{n+1} and an intermediate approximation v^* for the membrane potential (see Sundnes et al. 2005, for details). For solving these ODE systems we employ a third-order Singly Diagonally Implicit Runge Kutta (SDIRK) method with adaptive time stepping, as described in Sundnes et al. (2001).

2. Use $v(t_n) = v^*$ as initial condition and solve the linear PDE system

$$\nabla \cdot (\mathbf{M}_i \nabla v) + \nabla \cdot (\mathbf{M}_i \nabla u_e) = \frac{\partial v}{\partial t}, \quad (18)$$

$$\nabla \cdot (\mathbf{M}_i \nabla v) + \nabla \cdot ((\mathbf{M}_i + \mathbf{M}_e) \nabla u_e) = 0, \quad (19)$$

for $\mathbf{x} \in H$ and $t_n < t \leq t_{n+1}$, to obtain the transmembrane potential v_{n+1} and the extracellular potential $u_{e,n+1}$ at time t_{n+1}. A common approach is to solve these equations one by one in a sequential manner, as described in Skouibine et al. (2000) and Lines et al. (2002). However, we have chosen to discretise this system fully coupled, applying a backward Euler scheme in time and a Galerkin method in space. The resulting block-structured linear system is solved with a multigrid preconditioned conjugate gradient method, as described in Sundnes et al. (2002).

3. Employ the most recent value of the state vector $\mathbf{s}_{n+1}$ in the calculation of the active stress tensor $\mathbf{S}^{\mathrm{a}}$ and solve the nonlinear equilibrium equation

$$\nabla \cdot (\mathbf{F}(\mathbf{S}^{\mathrm{p}} + \mathbf{S}^{\mathrm{a}}(\mathbf{s}_{n+1}, \lambda, \dot{\lambda})) = \mathbf{0}, \quad \text{on } H(0), \quad (20)$$

to determine the new displacement vector field $\mathbf{u}_{n+1}$. This nonlinear equation is solved using Newton's method and a standard finite element spatial discretisation derived from the linearised weak form of (20) (see e.g. Holzapfel 2000 for a detailed derivation). Note that because the active stress depends strongly on the fibre stretch λ and its time derivative $\dot{\lambda}$, it is crucial that this part is updated for

every Newton iteration. Efficient techniques for updating and linearising the active stress component of recent cell contraction models are discussed in detail below.

The convergence of the complete numerical method will be governed by the accuracy of the splitting algorithm, as well as the accuracy of the solvers for the sub-problems. The Gauss–Seidel method and the Godunov splitting can be shown to be first order accurate methods. The convergence of the total algorithm is therefore limited to first order.

An additional advantage of operator splitting is the convenience of employing different spatial and temporal discretisations, to reflect the different scales of the subproblems. For the present problem we will use a relatively coarse mesh and time step for the mechanics part and for the communication between mechanics and electrophysiology, whereas the bidomain model is solved on a finer mesh and with smaller time steps. The electrophysiology solver is based on a geometric multigrid method (see Sundnes et al. 2002), and the mesh used for the mechanics equations is simply the coarsest mesh of the grid hierarchy. This approach facilitates the interpolations and restrictions necessary to communicate variables between the two subproblems. The cell equations in Step (1) are solved using an adaptive time step, which is very small in the upstroke phase and identical to the bidomain time step during the smoother time intervals (see Sundnes et al. 2001).

3.2 Discretisation and linearisation of active tissue mechanics

The main purpose of this study is to evaluate different techniques for solving the nonlinear elasticity problem defined by (20) and the constitutive relations (5)–(7), (13) and (14). The main challenges of this problem are related to the handling of active stress, because of its strong dependence on both deformation and the cellular states governed by (16) and (17). In essence, the challenge is to derive a stable and efficient time discretisation scheme for the differential-algebraic system composed by the ODEs (16) and (17) and the constraint (20).

3.2.1 Update methods for the active stress—The most intuitive approach to Step 3 of the algorithm above would be to insert the updated state vector $\mathbf{s}_{n+1}$ in (7) to compute $\mathbf{S}^{a}$, and then solve (20) for mechanical equilibrium while holding $\mathbf{S}^{a}$ fixed. As shown by Whiteley et al. (2007) and Niederer and Smith (2008), this approach leads to severe stability problems for all realistic models of cardiac contraction, because of the strong dependence of dynamic tension on strain and strain rate.

As shown by Niederer and Smith (2008), the stability problems can be resolved by re-calculating the dynamic tension for every Newton iteration using updated strain fields. With this approach, relations (5)–(7) may be viewed as a parameterised constitutive law for the heart tissue. For a given parameter $\mathbf{s}$, Equations (5)–(7) yield a unique relation between strains/strain rates and stresses. The update of dynamic tension is conveniently realised for the HMT model and related models (see Niederer et al. 2006). The reason is that these models formulate the active tension as a product of a tension depending on states $\mathbf{s}$, and scaling factors depending on λ and $\dot{\lambda}$. For these models the state-dependent tension may therefore be held constant over a time step, while the scaling factors are updated for every iteration.

A popular and fairly recent model for cardiac contraction is the model by Rice et al. (2008). The force development in this model is based on the cross-bridge distortion model of Razumova et al. (1999), which describes the cross-bridges as linear springs. The developed tension is proportional to the number of cross-bridges occupying strongly bound states, multiplied with their average distortion. Rice et al. (2008) assume the cross-bridges cycle through four states, out of which two contribute to tension development. This gives the following general behaviour of the dynamic tension:

$$F_{\text{active}} \propto XB_{\text{Pre } R}\, xXB_{\text{Pre } R} + XB_{\text{Post } R}\, xXB_{\text{Post } R}. \quad (21)$$

Here $XB_{\text{Pre } R}$ and $XB_{\text{Post } R}$ are fractions of cross-bridges in the strongly bound pre- and post-rotation states, and $xXB_{\text{Pre } R}$ and $xXB_{\text{Post } R}$ are their respective distortions. We refer to Rice et al. (2008) for a full description of the active tension and the remaining states of the model.

The critical variables in this context are the cross-bridge distortions $xXB_{\text{Pre } R}$ and $xXB_{\text{Post } R}$, as these are the variables mainly responsible for the deformation–force feedback. All other model variables, including $XB_{\text{Pre } R}$ and $XB_{\text{Post } R}$, are only weakly dependent on deformation, and are therefore easily adapted to the operator splitting scheme outlined above. The challenge of the distortion states is that they depend strongly on both deformation and state changes, as becomes evident from the governing ODEs:

$$\frac{\mathrm{d}}{\mathrm{d}t} xXB_{\text{Pre } R} = \frac{1}{2}\frac{\mathrm{dSL}}{\mathrm{d}t} + \frac{\phi}{XB_{\text{Pre } R}^{\text{Duty Fract}}}\left(-f_{\text{app } T}\, xXB_{\text{Pre } R} + h_{bT}\left(xXB_{\text{Post } R} - x_0 - xXB_{\text{Pre } R}\right)\right), \quad (22)$$

$$\frac{\mathrm{d}}{\mathrm{d}t} xXB_{\text{Post } R} = \frac{1}{2}\frac{\mathrm{dSL}}{\mathrm{d}t} + \frac{\phi}{XB_{\text{Post } R}^{\text{Duty Fract}}}\left(h_{fT}\left(xXB_{\text{Pre } R} + x_0 - xXB_{\text{Post } R}\right)\right). \quad (23)$$

The first terms on the right-hand sides of (22) and (23) represent the effect of sarcomere length changes ($\mathrm{SL} = \lambda \mathrm{SL}_0$) on cross-bridge distortion, whereas the rightmost terms represent distortion changes resulting from cross-bridge cycling. Here $f_{\text{app } T}$ and h_{bT} are constants; h_{fT} is a function of $xXB_{\text{Pre } R}$; φ and x_0 are constants and $XB_{\text{Pre } R}^{\text{Duty Fract}}$ and $XB_{\text{Post } R}^{\text{Duty Fract}}$ are steady-state solutions of cross-bridge states assuming full activation. See Rice et al. (2008) for a complete specification of these terms.

In this study we will investigate three different approaches to handling the deformation–force feedback mechanisms described by (22) and (23).

1. The first scheme is a modified version of the semi-implicit scheme proposed by Campbell et al. (2009) and Pathmanathan and Whiteley (2009). The idea is that when solving (20) for mechanical equilibrium, a subset of the ODEs is re-integrated over the most recent time step using the updated deformation state (λ and $\dot{\lambda}$). This will ensure that all deformation-dependent states are sufficiently updated. In Campbell et al. (2009), all states contributing directly to the active tension were re-integrated for every iteration ($XB_{\text{Pre } R}$, $XB_{\text{Post } R}$, $xXB_{\text{Pre } R}$ and $xXB_{\text{Post } R}$). In

order to minimise the book-keeping and communication between sub-problem solvers, we choose to reintegrate only the state variables that are strongly dependent on deformation ($xXB_{\text{Pre } R}$ and $xXB_{\text{Post } R}$). Hence, for every Newton iteration, (22) and (23) are re-integrated using a single forward Euler (FE) step, using the most recent value for SL and a finite difference approximation for dSL/dt. In the following, we will refer to this scheme as the FE method.

2. The second approach to be examined takes advantage of the particular structure of (22) and (23). We introduce new variables xSL, $xXB^{\text{s}}_{\text{Pre } R}$ and $xXB^{\text{s}}_{\text{Post } R}$, such that $xXB_{\text{Pre } R}=x\text{SL}+xXB^{\text{s}}_{\text{Pre } R}$ and $xXB_{\text{Post } R}=x\text{SL}+xXB^{\text{s}}_{\text{Post } R}$. The new variables are governed by

$$\frac{\text{d}}{\text{d}t}xXB^{\text{s}}_{\text{Pre } R}=\frac{\phi}{XB^{\text{Duty Fract}}_{\text{Pre } R}}\left(-f_{\text{app } T}\left(xXB^{\text{s}}_{\text{Pre } R}+x\text{SL}\right)+h_{bT}\left(xXB^{\text{s}}_{\text{Post } R}-x_0-xXB^{\text{s}}_{\text{Pre } R}\right)\right), \quad (24)$$

$$\frac{\text{d}}{\text{d}t}xXB^{\text{s}}_{\text{Post } R}=\frac{\phi}{XB^{\text{Duty Fract}}_{\text{Post } R}}\left(h_{fT}\left(xXB^{\text{s}}_{\text{Pre } R}+x_0-xXB^{\text{s}}_{\text{Post } R}\right)\right), \quad (25)$$

$$\frac{\text{d}x\text{SL}}{\text{d}t}=\frac{1}{2}\frac{\text{dSL}}{\text{d}t}. \quad (26)$$

The motivation for this splitting is that only xSL will be strongly dependent on deformation, so that the state-dependent variables $xXB^{\text{s}}_{\text{Pre } R}$ and $xXB^{\text{s}}_{\text{Post } R}$ can be kept constant through the Newton loop. Furthermore, (26) can be solved analytically to give

$$x\text{SL}=\frac{1}{2}(\text{SL}-\text{SL}_0),$$

where SL_0 is the initial sarcomere length. This variable is conveniently updated inside each Newton iteration. In the following, we will refer to this method as the xSL method.

3. The third update scheme is a modification of the first one. We observe that if we keep the rate function h_{fT} in (23) constant at its known value from time t_n, (22) and (23) become linear in $xXB_{\text{Pre } R}$ and $xXB_{\text{Post } R}$. If we also introduce the finite difference approximation $\text{dSL}/\text{d}t \approx(\text{SL}_{n+1}-\text{SL}_n)/\Delta t$, the resulting quasi-linear equations can be solved analytically. This solution method is often referred to as a generalised Rush–Larsen (GRL) scheme (Rush and Larsen 1978; MacLachlan et al. 2007), and gives explicit update formulas for $xXB_{\text{Pre } R}$ and $xXB_{\text{Post } R}$:

$$xXB^{n+1}_{\text{Pre } R}=xXB^{\text{ss}}_{\text{Pre } R}+\left(xXB^{\text{ss}}_{\text{Pre } R}-xXB^{n}_{\text{Pre } R}\right)\text{e}^{-\Delta t/\tau_{xXB_{\text{Pre } R}}}, \quad (27)$$

$$xXB^{n+1}_{\text{Post } R} = xXB^{\text{ss}}_{\text{Post } R} + \left(xXB^{\text{ss}}_{\text{Post } R} - xXB^{n}_{\text{Post } R}\right) \mathrm{e}^{-\Delta t/\tau_{xXB_{\text{Post } R}}}, \quad (28)$$

with the steady-state values and time constants given by

$$xXB^{\text{ss}}_{\text{Pre } R} = \frac{1}{2}\frac{\text{dSL}}{\text{d}t}\frac{XB^{\text{Duty Fract}}_{\text{Pre } R}}{\phi(f_{\text{app } T}+h_{bT})} + \frac{h_{bT}}{f_{\text{app } T}+h_{bT}}\left(xXB^{n}_{\text{Post } R} - x_0\right),$$
$$\tau_{xXB_{\text{Pre } R}} = \frac{XB^{\text{Duty Fract}}_{\text{Pre } R}}{\phi(f_{\text{app } T}+h_{bT})},$$
$$xXB^{\text{ss}}_{\text{Post } R} = \frac{1}{2}\frac{\text{dSL}}{\text{d}t}\frac{XB^{\text{Duty Fract}}_{\text{Post } R}}{\phi h_{fT}} + xXB^{n}_{\text{Pre } R},$$
$$\tau_{xXB_{\text{Post } R}} = \frac{XB^{\text{Duty Fract}}_{\text{Post } R}}{\phi h_{fT}}.$$

We see that the equations are updated one by one using the known value from time t_n for $xXB^{n}_{\text{Post } R}$ in the update of $xXB_{\text{Pre } R}$ and vice versa. The equations could also be solved as a system of two quasi-linear ODEs, which would require computing eigenvalues and eigenvectors of a two-by-two matrix. Although in certain cases this approach has been shown to give increased accuracy and stability, we have chosen to avoid this additional complexity. We will refer to this scheme as the GRL method.

All three update schemes treat the velocity term dSL/d*t* as constant over a time step and are in this respect similar to the update scheme proposed by Niederer and Smith (2008). However, as the formulation of velocity dependence is very different in Rice et al.'s (2008) model compared with Niederer et al.'s (2006), the update schemes also differ substantially. The performance of the three alternative update schemes is evaluated and compared below.

3.2.2 Linearisation of the active stress—All the update schemes outlined above lead to an active stress tensor that is a nonlinear function of the current strain. Any explicit dependence on strain rate ($\dot{\lambda}$) is avoided through a finite difference approximation that defines the strain rate as a function of current strain. For stable and efficient solution of (20), both the active and passive stress tensor in (5) must be linearised with respect to the displacement. The passive stress component S^p is derived from a strain energy function in the usual way, and the linearisation follows the standard steps from textbooks on nonlinear solid mechanics (see e.g. Holzapfel 2000). However, the formulation of the active stress is very different, and standard linearisation methods prove to be less suitable for this part.

Linearisation using the second elasticity tensor: The most common linearisation technique found in text books on nonlinear solid mechanics starts from (20) and proceeds to replace **F** and **S** by consistent linearisations around known states $\mathbf{F}_0$ and $\mathbf{S}_0$ along a direction $\Delta\mathbf{u}$:

$$\mathbf{F} \approx \mathbf{F}_0 + \frac{\partial \mathbf{F}}{\partial \mathbf{u}}\Delta u = \mathbf{F}_0 + \nabla(\Delta\mathbf{u}), \quad (29)$$

$$\mathbf{S} \approx \mathbf{S}_0 + \frac{\partial \mathbf{S}}{\partial \mathbf{u}} \Delta \mathbf{u} = \mathbf{S}_0 + \mathscr{C} \Delta \mathbf{E}. \quad (30)$$

Here $\nabla(\Delta \mathbf{u})$ is the gradient of the increment in the displacement field, whereas $\Delta \mathbf{E}$ is the increment in the Green–Lagrange strain (see, for instance, Holzapfel 2000, for a detailed discussion of the linearisation process). Furthermore, $\mathscr{C}$ is the *second elasticity tensor*, which is a fourth-order tensor that characterises the tangential stiffness of the tissue around the current stress state $\mathbf{S}_0$. Introducing vector-valued trial and test functions φ_i and φ_j, the approximations (29) and (30) lead to a stiffness matrix of the form

$$A_{ij} = \int_\Omega (\nabla \phi_i : \nabla \phi_j \mathbf{S}_0 + \mathbf{F}^T \nabla \phi_i : \mathscr{C} : \mathbf{F}^T \nabla \phi_j) \, \mathrm{d}\Omega. \quad (31)$$

The components of $\mathscr{C}$ are computed as partial derivatives of $\mathbf{S}$ with respect to the Green–Lagrange strain $\mathbf{S}$:

$$\mathscr{C}_{ijkl} = \frac{\partial S_{ij}}{\partial E_{kl}}.$$

For the passive elastic stress, given by (6), the second elasticity tensor is readily computed as second derivatives of the strain energy function:

$$\frac{\partial S^p_{ij}}{\partial E_{kl}} = \frac{\partial^2 \Psi}{\partial E_{ij} \partial E_{kl}}.$$

For the active component of the stress, the situation is more complicated. As seen in (7) the active stress is normally defined in terms of a Cauchy stress tensor, which is pulled back to the reference configuration. The differentiation of $\mathbf{S}^a$ with respect to components E_{ij} is complicated by the fact that the non-symmetric deformation gradient $\mathbf{F}$ contains more information than the symmetric Green–Lagrange strain $\mathbf{E}$. It is in general not possible to compute the components of $\mathbf{F}$ from the components of $\mathbf{E}$, and it is therefore difficult to differentiate $\mathbf{S}^a$ with respect to $\mathbf{E}$. A reasonable approximation may be obtained by differentiating $\boldsymbol{\sigma}^a$ with respect to the strains, and treating the deformation gradients in (7) as constants. However, as will be demonstrated below, this approach gives reduced convergence.

The standard linearisation technique is hence well suited for constitutive laws that are based on the second Piola–Kirchhoff stress tensor, but much less so for stress–strain laws that are naturally expressed in terms of the Cauchy stress or the first Piola–Kirchhoff stress.

Linearisation using the first elasticity tensor: For constitutive laws involving the Cauchy stress or the first Piola–Kirchhoff stress, which includes the most common models of the active stress component in the heart, it is more convenient to base the linearisation on a

slightly different formulation of mechanical equilibrium. The first Piola–Kirchhoff stress is given by **P** = **FS**, and consequently, (4) can be expressed as

$$\nabla \cdot \mathbf{P} = 0.$$

The linearisation of **P** around a known stress state $\mathbf{P}_0$ in the direction Δu can be written as

$$\mathbf{P} \approx \mathbf{P}_0 + \frac{\partial \mathbf{P}}{\partial \mathbf{u}} = \mathbf{P}_0 + \mathscr{A} \Delta \mathbf{F}, \quad (32)$$

where $\mathcal{A}$ is known as the *first elasticity tensor*, and defined as

$$\mathscr{A}_{ijkl} = \frac{\partial P_{ij}}{\partial F_{ij}}.$$

In the finite element framework, the linearisation in (32) leads to a stiffness matrix formulation in the following form:

$$A_{ij} = \int_\Omega \nabla \phi_i : \mathscr{A} : \nabla \phi_j \, \mathrm{d}\Omega. \quad (33)$$

For the active–passive decomposition of the stress that we employ in the heart muscle, $\mathcal{A}$ is naturally decomposed into two separate terms:

$$\mathscr{A}_{ijkl} = \frac{\partial P_{ij}}{\partial F_{ij}} = \frac{\partial P^{\mathrm{p}}_{ij}}{\partial F_{kl}} + \frac{\partial P^{\mathrm{a}}_{ij}}{\partial F_{kl}}.$$

The passive constitutive law is defined in terms of the Green–Lagrange strain and the second Piola–Kirchhoff stress, but the first term in $\mathcal{A}$ can still be computed easily by numerical differentiation of

$$\frac{\partial P^{\mathrm{p}}_{ij}}{\partial F_{kl}} = \frac{\partial \{F S^{\mathrm{p}}\}_{ij}}{\partial F_{kl}}.$$

As introduced above, the constitutive law for the active stress is normally given in terms of either first Piola–Kirchhoff or Cauchy stress, which are both easy to differentiate with respect to the components of *F*. For the active stress law applied above, which yields the active part of the second Piola–Kirchhoff stress as a pull-back of a Cauchy stress tensor, we first need to convert this to a first Piola–Kirchhoff stress,

$$\mathbf{P}^{\mathrm{a}} = \mathbf{F}\mathbf{S}^{\mathrm{a}} = J \boldsymbol{\sigma}^{\mathrm{a}}(s, \lambda, \dot{\lambda}) \mathbf{F}^{-T}.$$

Extracting the components of $\mathcal{A}_{iJkL}$ by numerical differentiation of this term with respect to **F** is trivial.

A mixed elasticity tensor: We have seen above that the active stress is most conveniently linearised using the first elasticity tensor, whereas both the first and second elasticity tensor may be applied for the passive stress component. Although in principle the two linearisation approaches are equivalent for the passive stress component, the use of numerical differentiation gives rise to small differences between the two formulations. Following the standard approach, a number of analytical steps are applied to arrive at the stiffness matrix formulation in (31), and numerical differentiation is applied only to establish the tensor C_{ijkl}. In the techniques based on the first elasticity tensor, the analytical steps are replaced by a single numerical differentiation step to achieve the stiffness matrix in (33). This is potentially less accurate and motivates the use of (31) whenever possible, and (33) only for the active stress component. Using this approach, the combined finite element stiffness matrix becomes

$$A_{ij}=\int_\Omega(\nabla\phi_i{:}\nabla\phi_j\mathbf{S}_0^{\mathrm{p}}+\mathbf{F}^T\nabla\phi_i{:}\mathscr{C}^{\mathrm{p}}{:}\mathbf{F}^T\nabla\phi_j+\nabla\phi_i{:}\mathscr{A}^{\mathrm{a}}{:}\nabla\phi_j)\,\mathrm{d}\Omega. \quad (34)$$

Here $\mathbf{S}_0^{\mathrm{p}}$ is the passive stress from the previous iteration, **F** is the deformation gradient from the previous iteration and $\mathcal{C}^{\mathrm{p}}$ and $\mathcal{A}^{\mathrm{a}}$ are the second elasticity tensor for the passive stress and the first elasticity tensor for the active stress, respectively.

4. Numerical results

In this section, we evaluate the performance of the three different semi-implicit update schemes outlined above, and the three alternative methods for linearising the active stress tensor.

4.1 Update schemes for active contraction

Stable update schemes for the HMT model and related contraction models were extensively studied in Niederer and Smith (2008). As noted above, we therefore focus on update schemes for the contraction model by Rice et al. (2008) and compare the performance of the three update methods outlined above (FE, *x*SL and GRL). The performance evaluation is based on a simplified test case, in which a single cell is stimulated and allowed to contract freely against a nonlinear elastic force. For this simplified deformation state, an incompressible form of (13) and (14) may be expressed in terms of λ and the hydrostatic pressure p:

$$\Psi=\frac{1}{2}C\mathrm{e}^{((b_{ff}+2b_{xx})\lambda^2)}-p(J-1).$$

The elastic force is assumed to be in parallel with the active contractile force, and assuming no external forces the equilibrium equation reduces to

$$\mathbf{S}^{\mathrm{p}}(\lambda, p)+\mathbf{S}^{\mathrm{a}}(\lambda, \mathbf{s})=0. \quad (35)$$

For **s** given, this is a system of two equations (zero stress in fibre and cross-fibre direction) and two unknowns (λ and p). The transverse component may be used to eliminate p and formulate the relation in terms of λ and **s** only. The system hence reduces to a differential-algebraic system consisting of ODEs (16) and (17) and a scalar constraint derived from (35). The material parameters are C = 0.876 kPa, b_{ff} = 20, b_{xx} = 4, T_{ref} = 125 kPa and γ_s = γ_n = 0.2.

The results of the test simulations are summarised in Table 1. The table shows the relative root mean square (RRMS) errors for all simulation schemes, using a reference solution based on the FE scheme and a very small time step. Computing the reference solution with any of the other schemes did not change the results significantly. The step sizes referred to in the table are the global time steps for the operator splitting scheme defined above, whereas the cell model ODEs are stepped forward using smaller internal steps. We see that the FE scheme, as applied here, suffers from severe stability problems, failing to converge for time steps larger than 0.1 ms. This problem could most likely be solved by taking several internal FE steps to update the cross-bridge distortions inside every Newton iteration, but due to the additional complexity associated with multiple internal steps, we did not investigate this further. The two other schemes both produce stable solutions at all choices of the global time step, and both methods appear to give first-order convergence. The accuracy of the two schemes is, however, significantly different, with the GRL scheme generally producing lower errors than the *x*SL scheme. This is illustrated further in Figure 1, in which we see that the *x*SL scheme converges very slowly, and does not produce satisfactory solutions for time steps of 5.0 and 1.0 ms.

4.2 Efficiency of linearisation methods

A second set of numerical experiments has been run to evaluate the linearisation methods for the combined active and passive stress tensors. We employ three different test cases: (i) active, free contraction of a tissue slab, as illustrated in Figure 2; (ii) passive inflation of the bi-ventricular geometry displayed in the left panel of Figure 3 and (iii) a complete, dynamic, heart cycle based on the same bi-ventricular geometry.

Case (i) is based on uniform activation and stress-free boundaries, making this 3D experiment very similar to the zero-dimensional case in Section 4.1. The left panel of Figure 2 shows the initial geometry (outline) and the maximally contracted slab (mesh). The initial dimensions are 5.0 × 0.5 × 0.5 cm^3, which is represented by a finite element mesh of 80 trilinear elements (20 × 2 × 2). The material parameters are set to C = 0.876 kPa, b_{ff} = 20, b_{xx} = b_{fx} = 4, T_{ref} = 55 kPa, C_{compr} = 100 kPa and γ_s = γ_n = 0.2. At maximal shortening the slab measures 3.71 × 0.56 × 0.56 cm. The volume reduction during contraction is approximately 7%, which is reasonably realistic for cardiac tissue. The right panel of Figure 2 shows the resulting fibre shortening. In Case (ii) the active stress is zero, reducing this example to a fairly standard case of nonlinear hyperelasticity, with the material law (13) and (14) and boundary conditions outlined in Section 2. The endocardial pressure is ramped from zero to a specified end diastolic pressure in 28 steps. For the left ventricle the end

diastolic pressure is set to 1.8 kPa, whereas for the right ventricle it is set to 0.7 kPa. Case (iii) is initiated with the same passive inflation as in (ii), but continues through the isovolumic contraction, ejection and isovolumic relaxation, employing the haemodynamic boundary conditions outlined in Section 2. For Cases (ii) and (iii), the mechanical material parameters are $C = 0.45$ kPa, $b_{ff} = 20$, $b_{xx} = 5$, $b_{fx} = 8$, $T_{\text{ref}} = 27.5$ kPa, $C_{\text{compr}} = 50$ kPa, $\gamma_s = 0.4$ and $\gamma_n = 0$. The finite element mesh consists of 6270 trilinear elements with 8088 nodes. The bidomain conductivities are as specified in Sundnes et al. (2006), but with the surface to volume ratio set to 1 cm^{-1}. The right panel of Figure 3 shows the resulting pressure volume loop.

The results of the four test cases are summarised in Table 2. The table shows the total Newton iterations and the normalised CPU times for the three different linearisation methods. For both cases of the actively contracting tissue slab, the linearisation based on the first elasticity tensor takes considerably fewer iterations than the standard approach. Although each iteration is slightly more expensive for the approach based on the first tensor, we still see a considerable reduction in CPU time. The mixed elasticity tensor gives exactly the same iteration numbers as the first elasticity tensor, but slightly higher CPU times due to the increased cost of computing two separate stiffness tensors.

As expected, we see that all three methods give very similar results for the passive inflation test case. In fact, the iteration numbers are identical for all three methods, which indicates that any roundoff error introduced by using the first elasticity tensor is insignificant. In terms of CPU time the mixed elasticity tensor gives the worst performance, since there is some overhead associated with computing two different elasticity tensors.

For the dynamic pressure–volume (PV) loop simulations in Case (iii), we see that the formulation based on the mixed elasticity tensor outperforms the other two in terms of number of iterations, while taking some additional CPU time compared with the method based on the first elasticity tensor. Linearisation based on the second elasticity tensor gives the worst performance both in terms of iterations and CPU time. Since this test case is the most realistic and relevant for our application, and also by far the most CPU demanding, we are led to the conclusion that linearisation based on the first elasticity tensor is the preferred method for actively contracting heart tissue. Any theoretical advantage offered by the mixed elasticity tensor seems to be outweighed by the additional cost of computing the two separate tensors.

5. Summary and discussion

We have presented an operator splitting algorithm for simulating strongly coupled cardiac electro-mechanics and discussed a number of challenges related to the stability and convergence of the active stress computations. Stability problems associated with operator splitting for strongly coupled simulations were analysed in detail in Niederer and Smith (2008), and a stable scheme based on a semi-implicit update scheme was presented. The scheme of Niederer and Smith was applicable for the HMT model and related models for cell contraction, for which the dynamic force is expressed as the product of an isometric force and a scaling factor accounting for the effect of deformation. We have extended the

discussion of semi-implicit update schemes to the widely used model from Rice et al. (2008), for which the form of the update scheme is less intuitive. We have proposed three different update schemes for Rice et al.'s model, and evaluated their performance for a simple test case. The results indicate that two of the solution schemes give stable solution for a wide range of time steps, but only the method based on the GRL scheme has sufficient accuracy for our application.

The introduction of semi-implicit schemes for active tension gives rise to additional challenges in linearisation of the stress equilibrium equation. The active stress component is typically given in terms of the Cauchy stress or first Piola–Kirchhoff stress, which makes it difficult to employ the most common linearisation technique used in nonlinear elasticity. This problem can be overcome by adopting a slightly different formulation of the stress equilibrium, and basing the linearisation on the first elasticity tensor. This improves the accuracy of the linearisation of active stress and leads to improved convergence of Newton's method.

A limitation of this study is the relatively small selection of models and test cases. We have chosen to focus on the contraction model by Rice et al. (2008), since this is widely used in the field and introduces additional challenges compared with earlier models based on the HMT model. The model is also representative for other recently developed contraction models (see e.g. Campbell et al. 2009). However, other models of cell dynamics may give rise to additional and different challenges that have not been addressed in this study. With the demonstrated performance of the GRL scheme, a particularly relevant study is to evaluate the applicability of this scheme for a wider range of active tension models. Furthermore, although we have chosen the numerical experiments to best highlight the performance differences between the methods, the conclusions may not be valid for all cases of realistic, strongly coupled electromechanics simulations. To the extent possible, more extensive studies based on highly refined and realistic test cases should form the basis for a choice of numerical method.

Although operator splitting has obvious advantages for the complex equation system describing coupled cardiac electro-mechanics, examples of fully coupled solution schemes are available in the literature (Göktepe and Kuhl 2009). Given the stability issues discussed both in Niederer and Smith (2008) and in this study, we may argue that the various update schemes and semi-implicit splitting methods should be replaced by a fully implicit solution method. A natural extension of this study would be to evaluate the performance of state of the art splitting methods against fully coupled solution schemes.

Acknowledgments

This research is supported by an Outstanding Young Investigators Award from the Research Council of Norway. This study is also supported by a Center of Excellence grant from the Norwegian Research Council to Center for Biomedical Computing at Simula Research Laboratory.

References

Campbell SG, Howard E, Aguado-Sierra J, Coppola BA, Omens JH, Mulligan LJ, McCulloch AD, Kerckhoffs RCP. Effect of transmurally heterogeneous myocyte excitation–contraction coupling on canine left ventricular electromechanics. Exp Physiol. 2009; 94(5):541–552. [PubMed: 19251984]

CellML web page. 2000–2012. [cited May 2012]. Available from: http://www.cellml.org

Göktepe S, Kuhl E. Electromechanics of the heart: a unified approach to the strongly coupled excitation–contraction problem. Comput Mech. 2009; 45(2–3):227–243.

Guccione J, Costa K, McCulloch A. Finite element stress analysis of left ventricular mechanics in the beating dog heart. J Biomech. 1995; 28(10):1167–1177. [PubMed: 8550635]

Gurev V, Lee T, Constantino J, Arevalo H, Trayanova NA. Models of cardiac electromechanics based on individual hearts imaging data: image-based electromechanical models of the heart. Biomech Model Mechanobiol. 2011; 10(3):295–306. [PubMed: 20589408]

Gurev V, Lee T, Constantino J, Arevalo H, Trayanova NA. Erratum to: models of cardiac electromechanics based on individual hearts imaging data. Biomech Model Mechanobiol. 2011; 10(3):307.

Holzapfel, G. Nonlinear solid mechanics: a continuum approach for engineering. Wiley; Chichester: 2000.

Holzapfel GA, Ogden RW. Constitutive modelling of passive myocardium: a structurally based framework for material characterization. Philos Trans Roy Soc A Math Phys Eng Sci. 2009; 367(1902):3445–3475.

Hunter P, McCulloch A, ter Keurs H. Modelling the mechanical properties of cardiac muscle. Progr Biophys Mol Biol. 1998; 69(2–3):289–331.

Kerckhoffs R, Bovendeerd P, Kotte J, Prinzen F, Smits K, Arts T. Homogeneity of cardiac contraction despite physiological asynchrony of depolarization: a model study. Ann Biomed Eng. 2003; 31:536–547. [PubMed: 12757198]

Kerckhoffs R, Neal M, Gu Q, Bassingthwaighte J, Omens J, McCulloch A. Coupling of a 3D finite element model of cardiac ventricular mechanics to lumped systems models of the systemic and pulmonic circulation. Ann Biomed Eng. 2007; 35(1):1–18. [PubMed: 17111210]

Lafortune P, Arís R, Vázquez M. Coupled electromechanical model of the heart: parallel finite element formulation. Int J Numer Meth Biomed Eng. 2012; 28:72–86.

Land S, Niederer S, Smith N. Efficient computational methods for strongly coupled cardiac electromechanics. IEEE Trans Bio-Med Eng. 2012; 59(5):1219–1228.

Lin D, Yin F. A multiaxial constitutive law for mammalian left ventricular myocardium in steady-state barium contracture or tetanus. J Biomech Eng. 1998; 120:504–517. [PubMed: 10412422]

Lines G, Buist M, Grøttum P, Pullan A, Sundnes J, Tveito A. Mathematical models and numerical methods for the forward problem in cardiac electrophysiology. Comput Vis Sci. 2002; 5(4):215–239.

Lines G, Grøttum P, Tveito A. Modeling the electrical activity of the heart: a bidomain model of the ventricles embedded in a torso. Comput Vis Sci. 2002; 5(4):195–213.

MacLachlan M, Sundnes J, Spiteri R. A comparison of non-standard solvers for ODEs describing cellular reactions in the heart. Comput Meth Biomech Biomed Eng. 2007; 10(5):317–326.

Nash M, Panfilov A. Electromechanical model of excitable tissue to study reentrant cardiac arrhythmias. Progr Biophys Mol Biol. 2004; 85:501–522.

Nickerson D, Smith N, Hunter P. A model of cardiac cellular electromechanics. Philos Trans Roy Soc London A. 2001; 359:1159–1172.

Nickerson D, Smith N, Hunter P. New developments in a strongly coupled cardiac electromechanical model. Euro-pace. 2005; 7:118–127.

Niederer S, Smith N. An improved numerical method for strong coupling of excitation and contraction models in the heart. Progr Biophys Mol Biol. 2008; 96(1–3):90–111.

Niederer S, Hunter P, Smith N. A quantitative analysis of cardiac myocyte relaxation: a simulation study. Biophys J. 2006; 90:1697–1722. [PubMed: 16339881]

Pathmanathan P, Whiteley JP. A numerical method for cardiac mechanoelectric simulations. Ann Biomed Eng. 2009; 37(5):860–873. [PubMed: 19263223]

Razumova MV, Bukatina AE, Campbell KB. Stiffness-distortion sarcomere model for muscle simulation. J Appl Physiol. 1999; 87(5):1861–1876. [PubMed: 10562631]

Rice J, de Tombe P. Approaches to modeling crossbridges and calcium-dependent activation in cardiac muscle. Progr Biophys Mol Biol. 2004; 85:179–195.

Rice JJ, Wang F, Bers DM, de Tombe PP. Approximate model of cooperative activation and crossbridge cycling in cardiac muscle using ordinary differential equations. Biophys J. 2008; 95(5):2368–2390. [PubMed: 18234826]

Rush S, Larsen H. A practical algorithm for solving dynamic membrane equations. IEEE Trans Biomed Eng. 1978; 25(4):389–392. [PubMed: 689699]

Skouibine K, Trayanova N, Moore P. A numerically efficient model for simulation of defibrillation in an active bidomain sheet of myocardium. Math Biosci. 2000; 166:85–100. [PubMed: 10882801]

Sundnes J, Lines G, Tveito A. Efficient solution of ordinary differential equations modeling electrical activity in cardiac cells. Math Biosci. 2001; 172(2):55–72. [PubMed: 11520499]

Sundnes J, Lines G, Mardal KA, Tveito A. Multigrid block preconditioning for a coupled system of partial differential equations modeling the electrical activity in the heart. Comput Methods Biomech Biomed Eng. 2002; 5(6):397–409.

Sundnes J, Lines G, Tveito A. An operator splitting method for solving the bidomain equations coupled to a volume conductor model for the torso. Math Biosci. 2005; 194(2):233–248. [PubMed: 15854678]

Sundnes, J.; Lines, G.; Cai, X.; Nielsen, B.; Mardal, KA.; Tveito, A. Computing the electrical activity in the heart. Springer-Verlag; Berlin Heidelberg: 2006.

Tung, L. A bidomain model for describing ischemic myocardial d.c. potentials. Cambridge, MA: Massachusetts Institute of Technology; 1978.

Usyk T, Mazhari R, McCulloch A. Effect of laminar orthotropic myofiber architecture on regional stress and strain in the canine left ventricle. J Elasticity. 2000; 61:143–164.

Usyk T, LeGrice I, McCulloch A. Computational model of three-dimensional cardiac electromechanics. Comput Vis Sci. 2002; 4:249–257.

Whiteley J, Bishop M, Gavaghan D. Soft tissue modelling of cardiac fibres for use in coupled mechano-electric simulations. Bull Math Biol. 2007; 69(7):2199–2225. [PubMed: 17453303]

Winslow RL, Rice J, Jafri S, Marbán E, O'Rourke B. Mechanisms of altered excitation-contraction coupling in canine tachycardia-induced heart failure, II: model studies. Circ Res. 1999; 84(5):571–586. [PubMed: 10082479]

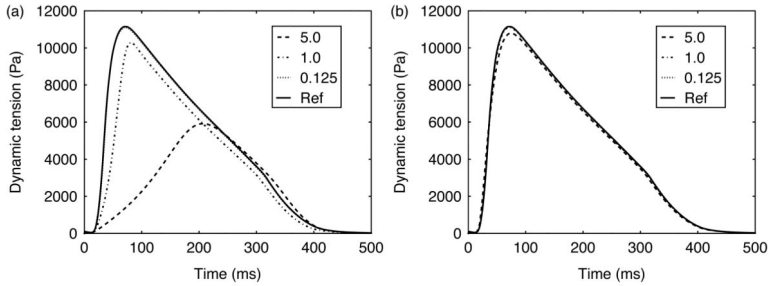

Figure 1.

Plots of developed dynamic force for three different time steps, using the *x*SL update method (left) and the GRL update method (right). The solid curve is the reference solution, whereas the dashed, dash-dotted and dotted curves are produced with 5.0, 1.0 and 0.125 ms, respectively.

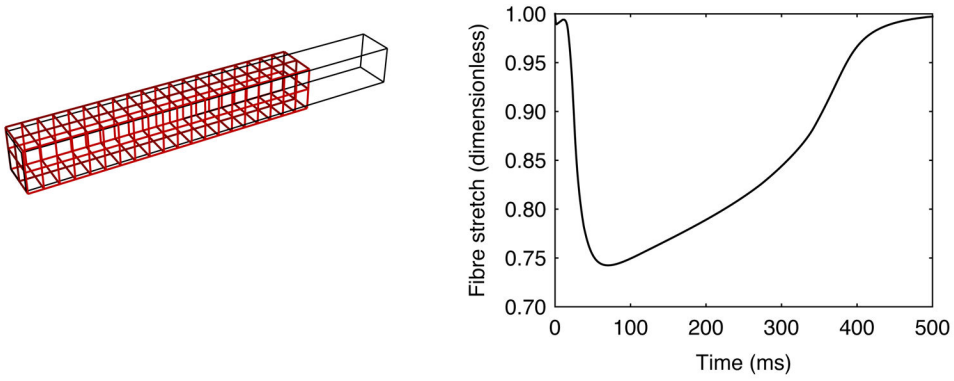

Figure 2.

Illustration of the active contraction tests using the thin slab geometry. The left panel shows the resting geometry (outline) and the fully contracted geometry (mesh). The right panel shows the time development of the fibre stretch ratio λ over a time course of 500 ms.

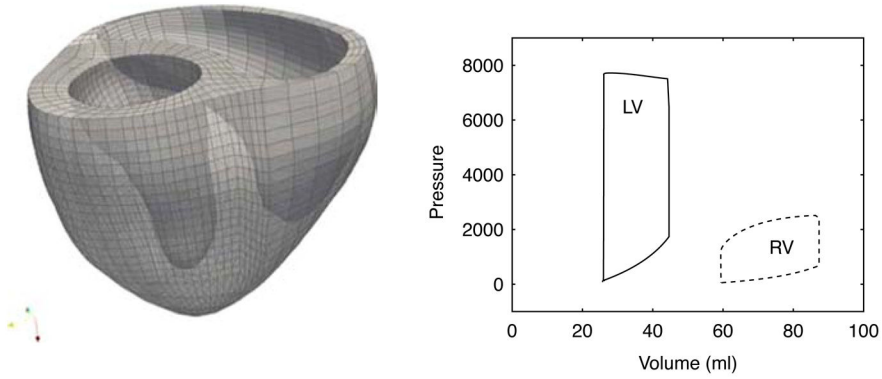

Figure 3.

Illustration of the test cases based on a human-sized bi-ventricular geometry. The left panel shows the computational grid used both for passive inflation and the complete, dynamic heart cycle. The right panel shows the PV loops obtained from the dynamic simulation.

Table 1

Convergence results for the three proposed numerical schemes for active force computations.

Δt	FE	*x*SL	GRL
5.0	–	0.66	0.037
1.0	–	0.22	0.0075
0.5	–	0.088	0.0034
0.25	–	0.030	0.0015
0.125	–	0.0085	0.00067
0.0625	0.00041	0.0045	0.00032

Note: The errors displayed are RRMS errors of the dynamic force.

Table 2

Comparison of the three alternative linearisation methods for four different test cases.

	1st tensor	2nd tensor	Mixed tensor
Free contraction of HMT	144 (1.0)	282 (1.55)	144 (1.19)
Free contraction of Rice et al.	174 (2.22)	227 (2.42)	174 (2.39)
Passive inflation	144 (87.3)	144 (87.3)	144 (103.6)
PV loop of Rice et al.	2326 (1168)	3416 (1562)	2184 (1345)

Notes: The total number of Newton iterations summed over all time steps, with the numbers in parentheses being normalised CPU times for the entire simulation.